



Foundry manufacturing of octave-spanning microcombs

JIZHAO ZANG,^{1,2}  HAIXIN LIU,^{1,2,*}  TRAVIS C. BRILES,¹  AND SCOTT B. PAPP^{1,2} 

¹Time and Frequency Division, National Institute of Standards and Technology, Boulder, Colorado 80305, USA

²Department of Physics, University of Colorado, Boulder, Colorado 80305, USA

*haixin.liu@colorado.edu

Received 6 May 2024; revised 5 August 2024; accepted 19 August 2024; posted 20 August 2024; published 6 September 2024

Soliton microcombs provide a chip-based, octave-spanning source for self-referencing and optical metrology. We use a silicon nitride integrated photonics foundry to manufacture 280 single-chip solutions of octave-spanning microcombs on a wafer. By group-velocity dispersion (GVD) engineering with the waveguide cross section, we shape the soliton spectrum for dispersive-wave spectral enhancements at the frequencies for f-2f self-referencing. Moreover, we demonstrate the other considerations, including models for soliton spectrum design, ultra-broadband resonator external coupling, low-loss edge couplers, and the nonlinear self-interactions of few-cycle solitons. To cover the fabrication tolerance, we systematically scan 336 parameter sets of resonator width and radius, ensuring at least one device on each chip can yield an octave-spanning comb with an electronically detectable carrier-envelope offset frequency, which has been supported by our experiment. Our design and testing process permit highly repeatable creation of single-chip solutions of soliton microcombs optimized for pump operation ~100 mW and high comb mode power for f-2f detection, which is the central component of a compact microsystem for optical metrology.

<https://doi.org/10.1364/OL.527540>

Kerr microresonator soliton frequency combs, or microcombs, have undergone rapid development because of the insights they provide to nonlinear dynamics and their application possibilities [1]. These broadband laser sources are composed of discrete spectral lines with the relation $f_n = nf_{\text{rep}} + f_{\text{ceo}}$, where n is an integer comb mode number, f_{rep} is the repetition frequency, and f_{ceo} is the carrier-envelope offset frequency. Several applications require phase stabilization of f_{rep} and f_{ceo} , including optical frequency synthesis [2] and measurement with respect to either microwave or optical clock signals, optical clock metrology, and optical frequency division [3].

Realizing a phase-stabilized microcomb involves generation of an octave-spanning spectrum with sufficient optical power for f-2f self-referencing and phase-locking of the f_{ceo} and f_{rep} signals [4–6]. Management of group-velocity dispersion (GVD) is critical for all of these tasks. The spectrum of a soliton microcomb is mostly determined by the integrated dispersion, $D_{\text{int}} = \nu_{\mu} - (\nu_0 + \text{FSR} \mu)$, where μ is the relative mode number to the pump mode, ν_{μ} is the cold cavity resonance frequency, and FSR is the free spectral range at the pump [7]. While dark

solitons in normal GVD have higher pump-to-comb conversion efficiency [8], bright solitons in anomalous GVD offer the broadest spectra, characterized by a bandwidth adjustable mostly with the second-order dispersion parameter and coherent emission of dispersive waves (DWs) [9–11] that arise due to higher-order dispersion. We consider dual DW microcombs with a shortwave DW (SWDW) and a longwave DW (LWDW) at higher and lower frequency than the pump laser, respectively. These DWs are designed according to the condition $D_{\text{int}} = 0$, and they greatly enhance the comb mode power and bandwidth. We control octave microcombs mostly by adjusting D_{int} with the resonator geometry. Indeed, the SWDW and LWDW are very sensitive to fabrication tolerance. Therefore, an approximate target design exists; however, to date it has only been implemented with carefully controlled, low-volume fabrication, requiring iterative device selection and fabrication or device trimming post-fabrication [12]. For frequency metrology, foundry manufacturing as a high-volume fabrication of f-2f microcombs would revolutionize the use of the SI second in the optical domain.

Here, we present a single-chip solution of microcombs with harmonic, dual DW spectra and electronically accessible f_{ceo} (~10 GHz) for the highest efficiency in f-2f detection and fabricate at a volume on a wafer with a commercial silicon nitride foundry. We model the target design through detailed SiN dispersion engineering, optimized microcomb dynamics that enhance DW power for f-2f detection, and wavelength-dependent external resonator coupling across octave span. A new feature of our modeling is an analytical expression for the complex, octave-spanning microcomb. To ensure every chip has qualified devices, each chip carries 336 resonators with a programmed variation in ring width (RW) and ring radius (RR) to account for the fabrication tolerance. Post-fabrication device screening in concert with our models is used to identify qualified devices on a single chip. We demonstrate that the two DW frequencies and f_{ceo} can be independently controlled in a predictable fashion sweeping resonator geometry. Finally, we discuss post-fabrication manipulation of the soliton spectrum through the control of the pump laser. This process reveals interesting DW dynamics that can lead to step-changes in the DW frequencies and power. Our work demonstrates a reliable procedure of generating ready-to-use octave-spanning combs through a commercial foundry and also expands the theory of the DW dynamics in soliton microcombs.

We first illustrate in Fig. 1 the procedure to obtain an octave-

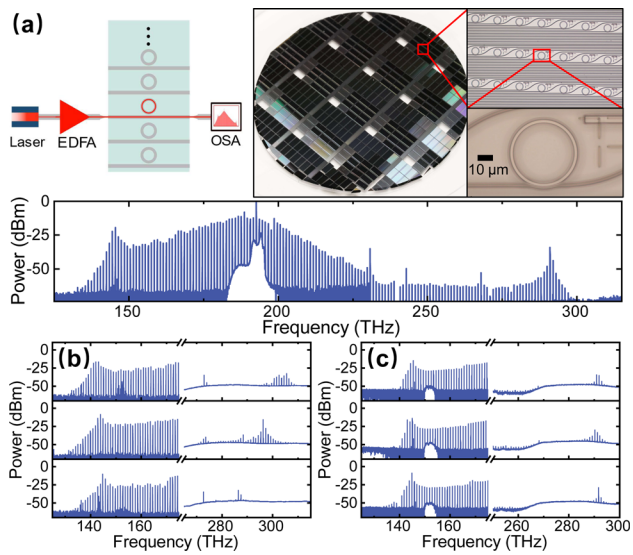


Fig. 1. Key concepts of chip-scale search for an octave-spanning comb from a commercial foundry. (a) Our chip testing setup (left) and photos of the wafer, a chip, and a resonator (clockwise from middle). The bottom spectrum shows an octave-spanning microcomb with an on-chip pump power of (151 ± 10) mW, RR of $23.475 \mu\text{m}$, and RW of 1690 nm. (b) and (c) Enlargements of DW spectra for different microresonator geometries. The DW locations are sensitive to RW (panel b; RW values: 1670 nm, 1690 nm, and 1710 nm) but less sensitive to RR (panel c; RR values: $23.475 \mu\text{m}$, $23.535 \mu\text{m}$, and $23.58 \mu\text{m}$). This allows DW control through RW and f_{ceo} control through RR .

spanning microcomb through chip-level device selection. The three essential parameters of our devices are layer thickness (th), RW , and RR . Before fabrication, our analytical model and simulation provided a suggested set of parameters: $th = 760$ nm, $RW = 1697$ nm, and $RR = 23.45 \mu\text{m}$. The devices were fabricated by Ligentec with a programmed variation in RW and RR around the suggested values. The upper inset of Fig. 1(a) shows chips on our wafer and individual devices (right side) and our experimental setup for soliton generation and device selection (left side). The pump from a C-band continuous-wave (CW) laser is amplified by an EDFA and coupled into a microresonator chip. The chip layer is made of silicon nitride and covered by silicon dioxide top cladding, providing low edge coupling loss (<3 dB per edge). By fast sweeping the pump frequency with a single-sideband suppressed-carrier (SSB-SC) frequency shifter, we achieve a stable access to the single soliton state without any feedback control and thermal compensation [13]. Then we finely adjust the detuning to optimize two DWs, monitored by an optical spectrum analyzer (OSA). The lower inset of Fig. 1(a) is a measured spectrum of an octave-spanning microcomb with two DWs at 145.43 THz and 290.92 THz, respectively. Figures 1(b) and 1(c) show more details about how we vary RW and RR to tune the DW frequencies and f_{ceo} for a workable octave-spanning microcomb. In Fig. 1(b), we fix RR and sweep RW from 1670 nm to 1710 nm, while in Fig. 1(c), we fix RW and sweep RR from $23.475 \mu\text{m}$ to $23.58 \mu\text{m}$. The measurement results indicate that the DW frequencies can be tuned by RW , and they are less sensitive to RR . On the other hand, f_{ceo} is sensitive to RR , which enables us to optimize f_{ceo} without changing the DW frequencies. Tuning RW also changes f_{ceo} but its influence can be easily counteracted by a relatively wide scan of RR values.

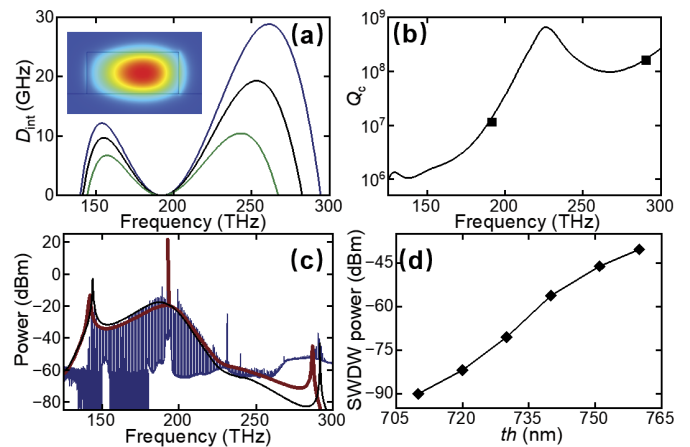


Fig. 2. Analytic model and simulation of comb spectrum. (a) Simulated D_{int} curves with $th = 760$ nm, $RR = 23.45 \mu\text{m}$, and $RW = 1670$ nm (blue), 1697 nm (black), and 1730 nm (green). The inset shows a typical ring mode profile. (b) Simulated (line) and measured (squares) Q_c versus frequency for $RR = 23.535 \mu\text{m}$, $WGW = 500$ nm, $g_c = 950$ nm, and $L = 17 \mu\text{m}$. (c) Comparison among measured comb spectra (blue), prediction from our analytic model (black) and LLE simulation (red) with $Q_i = 1.4M$, $F^2 = 37.2$, $\alpha = 33$. (d) SWDW power versus th , predicted by our analytic model with $F^2 = 37.2$ ($P_{\text{in}} = 150$ mW) and $\alpha = 33$. For each th , we adjust RW so that the two DWs span an octave.

With the programmed variation in microresonator geometries, we can identify microcombs with an electronically accessible f_{ceo} and enhanced DWs at frequencies for f-2f self-referencing.

Next, we will discuss the steps to generate a pre-fabrication design. We first regard th as a variable. To ensure an octave span, for each th , we find the proper RW by using COMSOL to calculate D_{int} since DWs appear at $D_{\text{int}} \approx 0$. Figure 2(a) shows the simulated D_{int} with varied RW . The inset shows a typical ring mode profile. The blue, black, and green curves plot the D_{int} with RW of 1670 nm, 1697 nm, and 1730 nm, respectively. For the black curve, two solutions of $D_{\text{int}} = 0$ span an octave, indicating that 1697 nm is the proper RW for this th .

After RW is determined, we design an optimal coupler that maximizes the coupling rate, denoted by $\kappa_{c\mu}$, at the SWDW, since $\kappa_{c\mu}$ is usually smaller at a short wavelength. The coupling is determined by three parameters: the bus waveguide width (WGW), the gap between the bus waveguide and the ring, g_c , and the pulley length, L . We use a Lumerical FDTD solver to simulate the coupling quality factor, defined by $Q_c = 2\pi\nu_\mu/\kappa_{c\mu}$, and find the best values of WGW , g_c , and L . The curve in Fig. 2(b) shows the simulated Q_c with $th = 751$ nm, $RR = 23.535 \mu\text{m}$, $RW = 1659$ nm, $WGW = 500$ nm, $g_c = 950$ nm, and $L = 17 \mu\text{m}$. The black squares are the measured Q_c with nominal RW and th to be 1690 nm and 760 nm, which agrees well with the simulation considering the fabrication uncertainty.

We now present a quasi-analytic model for solitons generated in resonators with arbitrary D_{int} profiles and use it to quantitatively predict the spectral mode distribution of the optical power, P_μ , given the device parameters and some estimation about the pump laser. This model is critical for obtaining a sufficient DW power for f-2f self-referencing. Here, we define a mode-dependent conversion efficiency $CE_\mu = P_\mu/P_{\text{in}}$, where P_{in} is the input pump power (≈ 150 mW in our experiment). P_μ can be estimated from CE_μ which is related to both the field

inside the resonator and the coupling. The intracavity dynamics of the Kerr microresonator is governed by the normalized Lugiato–Lefever equation (LLE) in mode basis [14]:

$$\frac{\partial E_\mu}{\partial t} = -(l_\mu + i(\alpha + D_\mu)) E_\mu + F\delta_{\mu,0} + i \sum_{\mu_1, \mu_2} E_{\mu_1} E_{\mu_2} E_{(\mu_1 + \mu_2 - \mu)}^* \quad (1)$$

Equation (1) is exactly the Fourier transform of the regular LLE in the temporal form, and the split-step Fourier method is used in its numerical solution. We account for the frequency-dependent loss in terms of the ratio of the loss rate between mode μ and the pump ($\mu = 0$), $l_\mu = (\kappa_{i\mu} + \kappa_{c\mu})/(\kappa_{i0} + \kappa_{c0})$, where $\kappa_{i\mu}$ is the intrinsic loss rate. α is the detuning of the pump laser, normalized by the half-width of the pump mode $(\kappa_{i0} + \kappa_{c0})/(4\pi)$. $D_\mu = 4\pi D_{\text{int}}/(\kappa_{i0} + \kappa_{c0})$ is the normalized D_{int} . F is the normalized driving force and related to P_{in} and P_{thre} by $F^2 = P_{\text{in}}/P_{\text{thre}}$, where P_{thre} is the threshold power and has a range of (4 ± 1) mW in the experiment.

The relation between coupling and CE_μ is characterized by $r_\mu = 2K_\mu/(K_\mu + 1)$, where $K_\mu = \kappa_{c\mu}/\kappa_{i\mu}$ is the coupling coefficient of mode μ , and CE_μ has the following form [14]:

$$CE_\mu = \frac{|E_\mu|^2 l_\mu r_\mu}{F^2/r_0} \times \frac{\omega_\mu}{\omega_0}, \quad (2)$$

where ω_μ is the output angular frequency of mode μ . As discussed above, $\kappa_{c\mu}$ can be calculated from Q_c . While Q_c varies greatly over frequency, the intrinsic quality factor $Q_i = 2\pi\nu_\mu/\kappa_{i\mu}$ has much smaller variation. We assumed Q_i to be a constant measured in previous fabrication. Then, l_μ and r_μ can be calculated from Q_c . Equation (2) suggests that we can calculate CE_μ if we know E_μ and F . In resonators with low loss and purely quadratic dispersion, $D_\mu = d_2 \mu^2/2$, the soliton spectrum is approximated by [15] the following:

$$E_\mu^{(0)} = \frac{\sqrt{d_2}}{2} \text{Sech} \left[\frac{\pi}{2} \sqrt{\frac{d_2}{2\alpha}} \mu \right]. \quad (3)$$

For non-quadratic dispersion, currently no model can approximate the soliton spectra. Here, we provide two extra orders of correction for E_μ which can characterize the spectrum around DWs through the perturbation method. To distinguish Eq. (3) from our correction, we denote it with a superscript (0).

Our model assumes that $D_\mu \approx d_2 \mu^2/2$ for small μ but diverges from the quadratic shape at large μ . For a steady comb, $\partial E_\mu/\partial t = i\lambda E_\mu$, where λ is the time rate of change of the phase and equals the difference between f_{rep} and FSR. For a D_{int} with even parity, $\lambda = 0$. We assume $\lambda = 0$ in our model but will discuss later that nonzero λ will result in a DW switching phenomenon. As a result, for nonzero μ , we rewrite Eq. (1) into the following:

$$E_\mu = \frac{\sum_{\mu_1, \mu_2} E_{\mu_1} E_{\mu_2} E_{(\mu_1 + \mu_2 - \mu)}^*}{-il_\mu + \alpha + D_\mu}. \quad (4)$$

With this equation, we can calculate our first-order solution $E_\mu^{(1)}$ by replacing E_μ on the right side with $E_\mu^{(0)}$. Instead of directly doing the summation, a more clever way is to notice that $E_\mu^{(0)}$ is a good approximation when D_μ is exactly $d_2 \mu^2/2$. So, according to Eq. (4), $\sum_{\mu_1, \mu_2} E_{\mu_1}^{(0)} E_{\mu_2}^{(0)} E_{(\mu_1 + \mu_2 - \mu)}^{(0)*} \approx (-il_\mu + \alpha + d_2 \mu^2/2) E_\mu^{(0)}$, and

$E_\mu^{(1)}$ has the following expression:

$$E_\mu^{(1)} = c_\mu^{(1)} E_\mu^{(0)}, \quad c_\mu^{(1)} = \frac{-il_\mu + \alpha + d_2 \mu^2/2}{-il_\mu + \alpha + D_\mu}, \quad (5)$$

where $c_\mu^{(1)}$ is the first-order correction. This expression already gives insight into comb power distribution across a dispersion profile. A striking feature of DWs is that P_μ has a local maximum at modes where $D_{\text{int}} \approx 0$. This is explained by Eq. 5: for most modes, $D_\mu \gg \alpha$, l_μ , and $|c_\mu^{(1)}|^2$ is relatively small, but when D_μ decreases to $-\alpha$, the line shape of $|c_\mu^{(1)}|^2$ becomes a Lorentzian with a peak value $\approx (d_2 \mu^2/(2l_\mu))^2$.

A more accurate spectrum needs the second-order correction:

$$E_\mu^{(2)} = E_\mu^{(0)} \frac{\sum_{\mu_1, \mu_3} c_{\mu_1}^{(1)} c_{\mu_3 - \mu_1}^{(1)*} c_{(\mu_3 - \mu)}^{(1)*} E_{\mu_1}^{(0)} E_{\mu_3 - \mu_1}^{(0)} E_{(\mu_3 - \mu)}^{(0)*} / E_\mu^{(0)}}{-il_\mu + \alpha + D_\mu}. \quad (6)$$

Note that $\text{Sech}[x] \leq 2 \text{Exp}[-|x|]$ and $|\mu_1| + |\mu_3 - \mu_1| + |\mu_3 - \mu| \geq |\mu|$. $E_{\mu_1}^{(0)} E_{\mu_3 - \mu_1}^{(0)*} E_{(\mu_3 - \mu)}^{(0)*} / E_\mu^{(0)}$ vanishes exponentially except for the case where $\mu \leq \mu_3 \leq \mu_1 \leq 0$ or $\mu \geq \mu_3 \geq \mu_1 \geq 0$, and $E_{\mu_1}^{(0)} E_{\mu_3 - \mu_1}^{(0)*} E_{(\mu_3 - \mu)}^{(0)*} / E_\mu^{(0)} \approx d_2$. Then $E_\mu^{(2)}$ can be expressed as follows:

$$E_\mu^{(2)} = c_\mu^{(2)} c_\mu^{(1)} E_\mu^{(0)}, \quad c_\mu^{(2)} = \frac{-il_\mu + \alpha + d_2 \sum_{\mu_1, \mu_3} c_{\mu_1}^{(1)} c_{\mu_3 - \mu_1}^{(1)*} c_{(\mu_3 - \mu)}^{(1)*}}{-il_\mu + \alpha + d_2 (|\mu| + 1)(|\mu| + 2)/2}, \quad (7)$$

where the summation is done over $\mu \leq \mu_3 \leq \mu_1 \leq 0$ or $\mu \geq \mu_3 \geq \mu_1 \geq 0$. In $c_\mu^{(2)}$, we retain $-il_\mu + \alpha$ in the numerator and replace $\mu^2/2$ with $(|\mu| + 1)(|\mu| + 2)/2$. This modification makes $c_\mu^{(2)}$ converge to 1 when $c_\mu^{(1)} = 1$.

Using Eqs. (2) and (7), we can calculate the spectrum of the output comb with given values of D_μ , l_μ , r_μ , F , α , and P_{in} . Equation (3) indicates that larger α leads to more power, as observed in the experiment as well. While absent from Eq. (7), F^2 affects P_μ indirectly by altering the soliton existence range, for which the upper bound of α is $\pi^2 F^2/8$ [15]. During the design, we set F based on our laser power and the measured P_{thre} and perform a numerical simulation with MATLAB, based on Eq. (1) directly, to estimate the maximum α and the comb spectrum more accurately. Figure 2(c) is a comparison among our analytic approximation (black curve), LLE simulation (red curve), and measured spectrum (blue trace) with nominal RW and th to be 1690 nm and 760 nm, respectively. For the analytic approximation and numerical simulation, we use the same device parameters as in Fig. 2(b) and Q_i is 1.4M. Considering the fabrication uncertainty, the analytic, simulated, and experimental spectra agree well.

The last parameter to optimize is th . We calculate the SWDW power versus th using our analytic model, shown in Fig. 2(d). Here, we set $RR = 23.45 \mu\text{m}$, $P_{\text{in}} = 150 \text{ mW}$, $F^2 = 37.2$, and $\alpha = 33$. RW is adjusted to keep an octave span of DWs. It shows that $th = 760 \text{ nm}$ will yield the highest SWDW power.

To compensate the th variation on the wafer and reduce f_{ceo} , we next decide sweep ranges of RW and RR based on the sensitivity of DWs and f_{ceo} . To characterize the harmonic mismatch between two DWs, we define the quantity $2\nu_L - \nu_S$, where ν_L and ν_S are LWDW and SWDW frequencies, and plot it as a function of RW and th with a fixed $RR = 23.5 \mu\text{m}$ [Fig. 3(a)]. The green, black, and red curves with diamonds show the theoretical values with $th = 754 \text{ nm}$, 760 nm , and 766 nm , respectively. The blue squares are calculated from the measured ν_L and ν_S . The plot shows that a 1 nm variation in th requires a 5 nm sweep in RW to compensate.

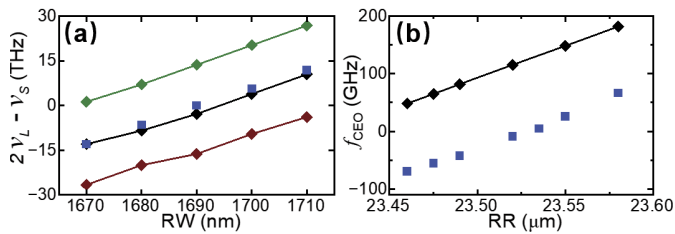


Fig. 3. Tuning of DW frequencies and f_{ceo} . (a) $2\nu_L - \nu_S$ versus RW for $th = 754$ nm (green), 760 nm (black), and 766 nm (red). The blue squares show the measured data for $th = 760$ nm. (b) Simulated (black curve with diamonds) and measured (blue squares) f_{ceo} as a function of RR .

Figure 3(b) plots the theoretical f_{ceo} (black curve with diamonds) and measured f_{ceo} over RR with $RW = 1690$ nm and $th = 760$ nm. We made this measurement with a 1 GHz resolution using a calibrated spectrometer, given the resolved comb modes. The lowest measured f_{ceo} is 5.1 GHz with $RR = 23.535$ μm and the corresponding spectrum is shown in Fig. 2(c). The similar slopes over RR highlight the accuracy of our prediction. The overall shift comes from the error in the effective index estimation. Since f_{ceo} is always less than FSR (~ 1 THz), we sweep 48 RR values over a range of 0.8 μm , which will always compensate the overall shift and enable an f_{ceo} below ± 10 GHz.

Besides device design, we can also use post-fabrication methods to manipulate the soliton spectrum through the control of the pump laser. Here, we investigate how α and P_{in} affect DWs and the DW switching phenomenon. According to Eq. (3), α determines the attenuation rate of P_μ versus μ . In addition, we found both in the experiment and simulation that DWs might switch from one mode to another nearby mode during the detuning sweep, enabling fine tuning of DW frequencies. This behavior comes from the nonlinear self-interactions between DWs and its parent soliton, causing f_{rep} to diverge from FSR [16], namely, $\lambda \neq 0$, which can be regarded as an effective shift in D_{int} and switches DW modes. In Fig. 4(a), we plot three LLE-simulated spectra with varied α : 19 (blue), 26 (green), and 33 (red) ($F^2 = 37.2$). The simulated comb power P_{comb} versus α is shown in Fig. 4(b), where the corresponding α for each spectrum in Fig. 4(a) is indicated by diamonds in the same color. Each

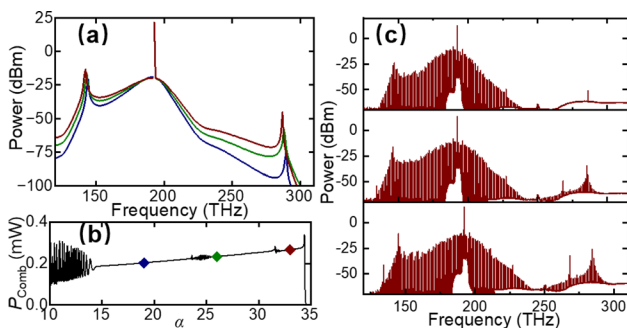


Fig. 4. Dependence of the comb spectrum on the pump laser. (a) Simulated soliton spectra with $F^2 = 37.2$, $\alpha = 19$ (blue), 26 (green), and 33 (red) using resonator parameters from Fig. 2(c) except α . (μ_L, μ_S) are $(-51, 102)$ (blue); $(-52, 100)$ (green); and $(-53, 99)$ (red). (b) Simulated comb power as a function of α . Each colored diamond corresponds to the soliton spectrum with the same color in (a). (c) Measured soliton spectra with the same devices but different P_{in} : 74 mW (top), 89 mW (middle), and 126 mW (bottom).

comb is a stable solution of LLE and we have experimentally verified that these states correspond to low noise combs. The relative mode numbers of DWs (μ_L, μ_S) switch from $(-51, 102)$ (blue) to $(-52, 100)$ (green) and then to $(-53, 99)$ (red). In contrast to quadratic GVD combs, P_{comb} does not increase smoothly in Fig. 4(b). Instead we observe that P_{comb} versus α behavior is interrupted by high noise regions around $\alpha = 25$ and 32 , related to the intracavity dynamics of DWs that cause jumps of the DW frequency and power [16].

P_{in} also affects CE_μ by affecting the range of α where the soliton exists. Figure 4(c) plots the three measured spectra from the same device but with increasing P_{in} : 74 mW, 89 mW, and 126 mW. For each P_{in} , we tuned α to maximize the SWDW power in the experiment. While P_{in} increases by less than two times, the SWDW power increases by tens of dB, which we attribute to a larger α able to support the soliton.

In summary, with a commercial foundry, we demonstrate a systematical design process and chip-scale search method to obtain single-chip solutions of microcombs for f-2f self-referencing at volume. We tested three chips from different parts of the wafer. Each includes octave-spanning combs with electronically accessible f_{ceo} . The variation in the DW power is about 10 dB. We also provide an analytical model to predict the soliton spectrum with two DWs and investigate its dependence on the device parameters as well as the pump laser. The experiment results agree well with analytical model and LLE simulations. Our work represents an important step toward the practical applications of the microresonator-based octave-spanning combs for self-referencing.

Funding. National Institute of Standards and Technology; National Science Foundation (OMA – 2016244); Defense Advanced Research Projects Agency (DODOS); Air Force Office of Scientific Research (FA9550-20-1-0004).

Disclosures. The authors declare no conflicts of interest.

Data availability. Data underlying the results presented in this paper are not publicly available but may be obtained from the authors upon reasonable request.

REFERENCES

1. T. J. Kippenberg, A. L. Gaeta, M. Lipson, *et al.*, *Science* **361**, eaan8083 (2018).
2. D. T. Spencer, T. Drake, T. C. Briles, *et al.*, *Nature* **557**, 81 (2018).
3. S. Sun, B. Wang, K. Liu, *et al.*, *Nature* **627**, 540 (2024).
4. H. Telle, G. Steinmeyer, A. Dunlop, *et al.*, *Appl. Phys. B* **69**, 327 (1999).
5. P. Del'Haye, T. Herr, E. Gavartin, *et al.*, *Phys. Rev. Lett.* **107**, 063901 (2011).
6. Y. Okawachi, K. Saha, J. S. Levy, *et al.*, *Opt. Lett.* **36**, 3398 (2011).
7. J. A. Black, G. Brodnik, H. Liu, *et al.*, *Optica* **9**, 1183 (2022).
8. J. Zang, S.-P. Yu, H. Liu, *et al.*, "Laser-power consumption of soliton formation in a bidirectional Kerr resonator," *arXiv* (2024).
9. M. H. P. Pfeiffer, C. Herkommer, J. Liu, *et al.*, *Optica* **4**, 684 (2017).
10. V. Brasch, M. Geiselmann, T. Herr, *et al.*, *Science* **351**, 357 (2016).
11. Q. Li, T. C. Briles, D. A. Westly, *et al.*, *Optica* **4**, 193 (2017).
12. G. Moille, D. Westly, E. F. Perez, *et al.*, *APL Photonics* **7**, 126104 (2022).
13. J. R. Stone, T. C. Briles, T. E. Drake, *et al.*, *Phys. Rev. Lett.* **121**, 063902 (2018).
14. H. Liu, G. M. Brodnik, J. Zang, *et al.*, *Phys. Rev. Lett.* **132**, 023801 (2024).
15. T. Herr, V. Brasch, J. D. Jost, *et al.*, *Nat. Photonics* **8**, 145 (2014).
16. D. V. Skryabin and Y. V. Kartashov, *Opt. Express* **25**, 27442 (2017).